Real-Time Water-to-Air Communication System Under Dynamic Water Surface and Strong Background Radiation

Tianrui Lin [ID], Tianjian Wei, Qingqing Hu [ID], Chunfang Fu, Nuo Huang [ID], Xinhui Liu, Li Tang, Liang Su, Jianghua Luo, and Chen Gong [ID], *Senior Member, IEEE*

Abstract—This work explores water-to-air optical wireless communication (W2A-OWC) transmission schemes and realizes a prototype of real-time W2A-OWC system based on field programmable gate array. This prototype comprises underwater nodes, aerial nodes, and transmitter-receiver hardware circuits. The real-time system employs multiple-input multiple-output technique and the low density parity check (LDPC) code of 5G-new radio for dynamic W2A-OWC. Additionally, the impact of background radiation is mitigated through spatial optical filtering. To validate the practical feasibility of the system, experiments are conducted in both indoor water tank and outdoor deep pool under strong background radiation. The frame error rate of the real-time system is tested under different LDPC code rates and transmitter-receiver configurations. The experimental results verify the feasibility of the realized W2A-OWC system.

Index Terms—Dynamic water-air surface, multiple-input multiple-output, real-time system, water-to-air optical wireless communication.

I. INTRODUCTION

EFFICIENT and reliable data transmission from oceanic environments necessitates a robust water-to-air (W2A) communication system, a topic that has garnered significant interest in both academic and industrial fields [1]. The traditional strategy for W2A communication, which uses a floating buoy relay on the water surface, suffers from weak flexibility, poor confidentiality, and high overhead, limiting the scalability of the system [2], [3], [4].

Requirements for more practical approaches motivate us to establish a direct and stable communication link between underwater nodes (e.g., underwater unmanned vehicles and sensors) and terrestrial nodes (e.g., unmanned aerial vehicles and base stations). It is necessary to find a suitable carrier that allows the signal to propagates through the water, water-air interface and atmosphere between the transmitter and the receiver. There are three typical carriers: acoustic wave, radio frequency (RF) wave, and optical wave [5]. Acoustic wave, traditionally favored for underwater communication, offers extended transmission distances in water, reaching several kilometers. However, it falls short in supporting high-speed applications due to the limited bandwidth and substantial latency [6]. Additionally, the water-air interface reflects a significant portion of the acoustic wave energy, leading to pronounced attenuation [3]. Besides, the size and power requirements of acoustic devices further detract from their economic viability in large-scale deployments. On the other hand, RF signals can cover extensive distances and achieve high transmission rates, reaching up to tens of kilometers and hundreds of Mbps in the air. The critical weaknesses of RF wave lie in the severe absorption and attenuation in underwater environments, although bands with smaller attenuation are found within the range of extremely low frequency to very low frequency. It is difficult for the system to achieve satisfactory transmission rate and the transmission distance [7].

The evolution of optical wireless communication (OWC) has recently highlighted its promising capabilities, particularly in enabling high-speed and efficient medium-range communication across the water-air interface. Firstly, the attenuation of light with wavelengths in the blue-green window is acceptable in both the atmosphere and water, which means that optical wave can achieve relatively long transmission distance over W2A link. Secondly, only a small fraction of the optical wave energy is reflected at the water-air interface (about 5% at vertical incidence). Thirdly, OWC allows the use of low-cost and miniaturized light-emitting diodes (LEDs) and photodetectors for high data rate, which facilitates the large-scale deployment of W2A communication networks. These advantages make OWC an ideal candidate for future W2A communication applications.

W2A-OWC offers many benefits, but it also introduces substantial challenges. The performance of W2A-OWC system in real scenarios suffer from weak signals, strong background

radiation, and high link dynamics. These channel characteristics bring higher demands on the implementation of the real-time W2A-OWC system.

Over the past few years, extensive studies have been carried out for W2A-OWC, mainly including channel characterization and system realization. The link gain and delay of W2A-OWC were evaluated by Monte Carlo simulations to show the influence of dynamic environment [8], [9]. Work [10] demonstrated that small-scale wave mainly affects the energy distribution and the variation frequency of link gain, while large-scale wave mainly affects the coverage area. The efficiency of W2A-OWC is improved through high-order modulation or wavelength-division multiplexing [11], [12], [13], [14]. In addition, mitigating the interference caused by random wave refraction via active or passive strategies is also an important technical direction. Work [10] shows that notable performance enhancement can be achieved by deploying more transmitters or receivers and increasing the distance between the transmitters or receivers. In works [15] and [16], beam tracking was employed to alleviate communication degradation induced by wave. Furthermore, "AmphiLight" employed an ultrasonic array to reconstruct the water surface and predict channel, thereby enabling bidirectional W2A-OWC [17]. Several works focus on the application of different wavelengths and different modulation modes in W2A-OWC [18], [19]. Work [18] shows that near-infrared wavelength exhibits greater resilience to the aqueous suspension particles with a smaller scattering effect. Work [20] shows that ultraviolet wavelength can facilitate the establishment of non-line-of-sight W2A communication link based on its potent scattering properties.

In this study, we develop a real-time W2A-OWC system with variable code rate. This system adopts a multi-transmitter and multi-receiver configuration. Extensive tests has been conducted in both laboratory tank and outdoor deep pool. The key contributions are:

- An integrated and flexible real-time system has been developed. This system meticulously combines several components at both the transmitter and receiver, including the underwater node, spatial optical filters, arrays of LEDs and avalanche photodiodes (APDs), a digital signal processing system based on field programmable gate arrays (FPGAs). Additionally, the multiple-input multiple-output (MIMO) technique and low density parity check (LDPC) code of 5G-new radio (NR) with variable code rate are introduced into the developed real-time communication system for dynamic environment.
- Real-time experiments are conducted in both laboratory tank and outdoor deep pool. Laboratory experiments have verified that the 4×4 MIMO system significantly reduces the frame error rate (FER) compared to the SISO system. Notably, with a code rate of 0.846, the FER decreases from 99% to 57.55%; and with a code rate of 0.55, the FER falls from 92.16% to 16.65%. To our knowledge, this is the first implementation of a real-time and MIMO-based W2A-OWC system that operates with zero frame error in outdoor tests at the distances of 3 m above water and 5 m underwater.

Work [21] demonstrated a bi-directional throughput of 5 Mbps with zero bit error rate (BER), achieving distance of up to 6.1 m in strong ambient light condition. Additionally, it shows improvement in connection time ranging from 47.1% to 29.5% under wavy water surface. The distinctions between our research and [21] are as follows. Firstly, work [21] employs an ultrasonic array to reconstruct the water surface and ensures alignment between the transmitter and receiver by varying the incident position of laser beam on the water surface. The reliability of this system is constrained by the accuracy of the reconstruction algorithm and the response time. In scenarios where the channel state changes rapidly, the system performance may be limited. In contrast, our approach, which combines MIMO technology with LDPC coding, exhibits stronger robustness under dynamic water surface conditions. Secondly, work [21] utilizes lasers and silicon photomultipliers with narrow bandpass filters as light sources and detectors; while this work adopts less expensive components, such as LEDs and APDs as light sources and detectors, respectively. Thirdly, work [21] acquires received data using high-speed oscilloscope for offline processing, whereas we realize a real-time system based on FPGA platform, which is crucial for future integration and commercialization. Finally, we achieve error-free frame transmission up to 5 m underwater and 3 m in the air, even in dynamic water surface and strong background radiation conditions. This is the longest distance reported for outdoor W2A-OWC to date.

The remainder of this paper is organized as follows. Section II describes the transmitter component of the developed real-time W2A-OWC system, receiver component of the developed real-time W2A-OWC system and signal processing procedure are described. Section III presents the test results of the proposed real-time system in the laboratory tank and outdoor deep pool. Finally, Section IV concludes this paper.

II. REAL-TIME SYSTEM MODELING

We describe the components of the developed W2A-OWC real-time system, including the architectures of aerial and underwater nodes, along with the associated software and hardware components.

In W2A-OWC applications, the underwater nodes are generally situated at depth ranging from several meters to tens of meters. Due to alignment challenges between underwater and aerial nodes, adopting a light source with a wide divergence angle is crucial to ensure that the receiver falls within the coverage area, at the cost of increased attenuation of the received signal. To relieve such issue and mitigate the signal fluctuation due to dynamic water surface, a diversity transmitter and receiver scheme is adopted. In our previous work [10], we generated various types of waves in the laboratory and validated that small-scale waves on the water surface, such as ripples and local fluctuations, significantly impact the propagation path of optical signal and the dynamic nature of link gain within a small spatial range. Therefore, even for two pairs of transceivers located close to each other, the channel variations may differ completely. Moreover,
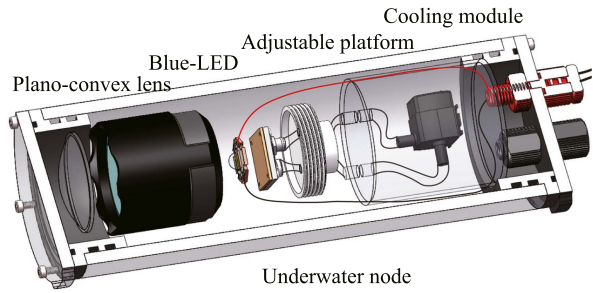
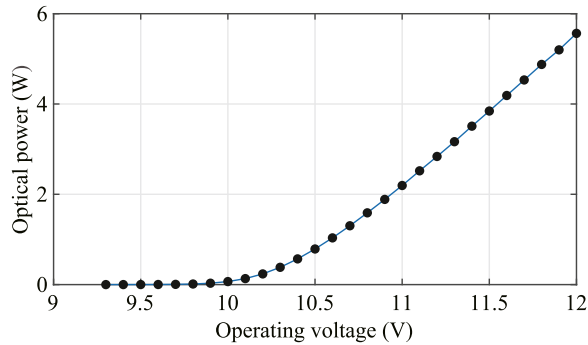Fig. 1.   Schematic diagram of a single underwater node.

Fig. 2.   The output optical power of LED versus operating voltage.

Fig. 3.   The optical power density versus beam divergence angle.

incorporating additional receivers diminishes the requirement for precise alignment between transmitters and receivers.

We adopt a coding strategy based on the 5G-NR LDPC protocol, enabling the system to operate under various code rates and thus allowing for a balance between transmission efficiency and reliability according to water quality, background radiation intensity and transmission distance.

A. Transmitter Realization

The transmitter component, shown in Fig. 1, uses M high-power blue LEDs (CREE XHP70) as the light sources. Due to the wide beam angle, the coverage area and signal reception can be enhanced. Fig. 2 presents the "optical power-operating voltage" curve for the blue LEDs utilized in our system. The optical power is measured using an optical power meter (Thorlabs PM100D with sensor S130 C). The LED in each underwater node operates at an optical power of 1.9 W under a DC voltage of 10.8 V.

To mitigate the challenges associated with the use of high-power LEDs, including increased heat generation, reduced efficiency, and potential thermal drift that could impair signal quality, a water cooling module (12 V, 9 W) is integrated into the underwater node. The LED chip is affixed to a heat sink to guarantee stable and extended signal acquisition. Additionally, a plano-convex lens with a focal length of 5 cm is positioned in front of the LEDs to adjust the beam divergence angle and spot coverage. The divergence angle of the LED beam, as measured, can be adjusted from $10°$ to $75°$. Fig. 3 illustrates the relationship between optical power density and beam divergence angle. The transmitter is encased in a transparent acrylic container, secured by a flanged joint for effective waterproofing.
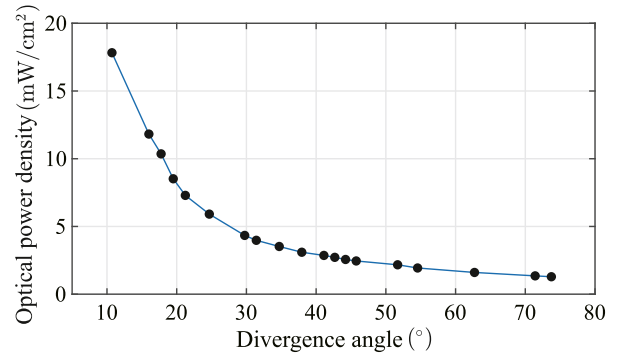
The intensity of LED light is controlled by both the FPGA and host computer. The FPGA contains a 2-channel digital-to-analogue converter (DAC) module. Subsequently, the signal is divided into four channels by two power splitters, enabling the simultaneous driving of four LEDs. Additionally, the onshore platform is connected to the underwater node via a waterproof cable.

B. Receiver Realization

In outdoor OWC, the performance degradation of the receiver optoelectronic device due to background radiation is a significant concern. In W2A-OWC scenario, the receiver is positioned in an aerial node with its photosensitive area facing downwards. Consequently, most of the background radiation received by the receiver results from the reflections of solar radiation from the water surface. The solar elevation angle θ_{sh} and the solar azimuth angle ϕ_{sh} are commonly adopted to characterize the relative position of the Sun, as shown in Fig. 4(a). We simulate the arrival angle of solar radiation on the receiving plane using Monte Carlo method. The specific simulation process is provided in [10]. Despite the randomness of the dynamic water surface, the angle between the solar radiation and the normal to the photosensitive area of receiver is strongly correlated with the incidence angle of the sunlight on the water surface. Fig. 4(b) and (c) show the statistical distribution of the angles at which solar radiation reaches the receiver for various solar elevation angles. The results indicate that the average arrival angle of solar radiation is very close to the complementary angle of the solar elevation angle.

Therefore, a dual strategy that combines field-of-view (FOV) control and light filtering is implemented. As shown in Fig. 5, an optical antenna, consisting of a light cup, apertures A ($\varnothing$ 2.3 mm–$\varnothing$ 49 mm) and B ($\varnothing$ 1.0 mm–$\varnothing$ 18 mm), is placed in front of the APD (Hamamatsu C12702-12, 3-dB bandwidth 4 kHz–40 MHz and photosensitivity 8.1 A/W in 460 nm). The light cup ($\varnothing$ 60 mm, height 35 mm) eliminates stray light caused by atmospheric and underwater scattering, while the apertures work together to adjust the APD FOV and filter out the intensive background component.

The front-end bandpass filter at the APD matches the central wavelength of the transmitter, significantly enhancing signal
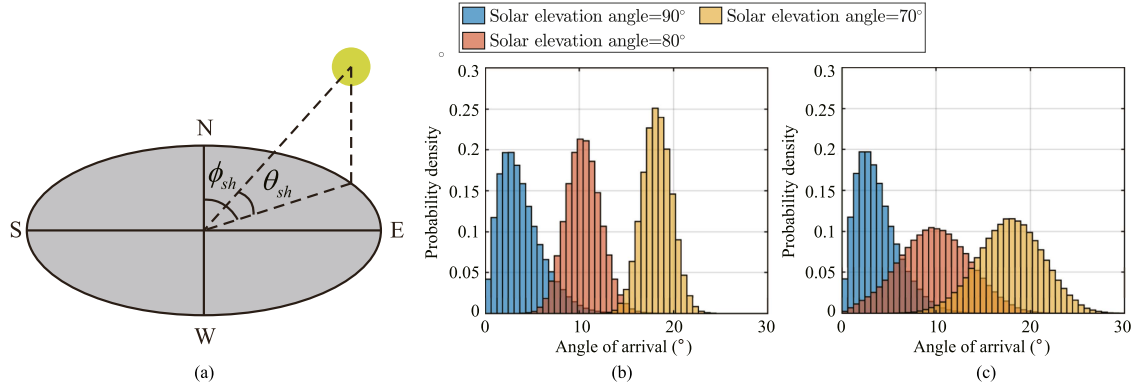
Fig. 4. (a) Solar elevation angle and solar azimuth angle. (b) The distribution of the angle of arrival of background radiation at the receiver when $\phi_{sh} = 0°$. (c) The distribution of the angle of arrival of background radiation at the receiver when $\phi_{sh} = 90°$.
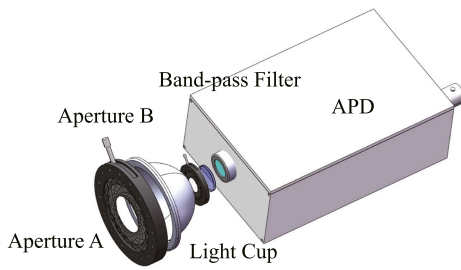

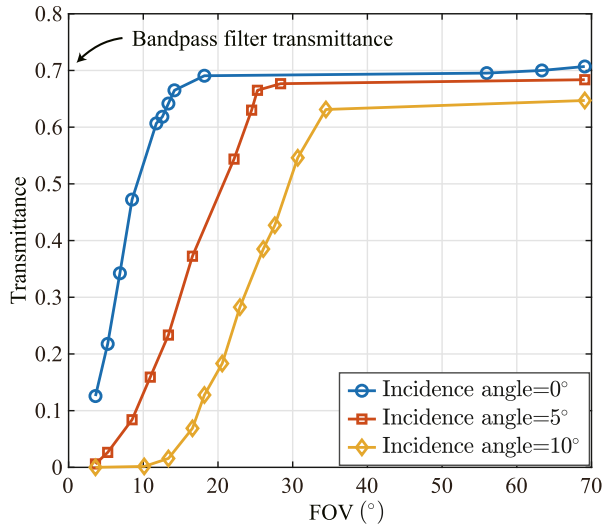Fig. 5. Schematic diagram of a single aerial node.

Fig. 6. The transmittance of the designed optical antenna versus FOV for different incidence angles.

separation against the background interference at other wavelength. The relationship between the transmittance of the designed optical antenna and FOV for different incidence angles is shown in Fig. 6.

To enhance stability and ensure consistent spacing under various experimental conditions, the APD arrays are rigidly connected using a strong alloy structure. This configuration reinforces the structural integrity of APD array, protecting against potential misalignment of the individual APDs.

C. Signal Processing

Fig. 7 shows the procedure of data processing in the real-time system. The serial port of computer transmits original data to the FPGA development board (ALINX AX7021) via a USB-to-TTL serial module (CH343 G), which is stored in the first-in-first-out (FIFO) queue. When the data in the FIFO queue accumulates to the specified bit length, a preliminary 32-bit information block is added, containing details like the code rate, modulation method, as well as the original and destination addresses. Subsequently, 24-bit cyclic redundancy check (CRC) bits are attached to the data, which is then sent to the LDPC coding IP core for encoding. The encoded data is attached to the 255-bit synchronization sequence, creating a complete data frame. Subsequently, this frame data undergoes rate conversion and is modulated into an on-off keying (OOK) signal. Finally, the signal is outputted through a 14-bit DAC (ALINX, AN9767). The output of the DAC is divided by power splitter (Mini-Circuits, ZFSC-2-4-S+) and connected to an LED array for signal transmission via a bias-tee that interfaces with direct current (DC) voltage (Rigol, DP832 A, operating voltage = 10.8 V). The signals emitted by the LED array travel through the water, cross the water-air interface, and propagate in the atmosphere before reaching the receiver.

The optical signal passes through the FOV cone delineated by apertures A and B, and subsequently through a filter, before reaching the photosensitive area of APD. Such configuration effectively filters out most background radiation prior to its arrival at the receiver. The optical signal is converted into the corresponding electrical signal by the APD. The signal then passes through the low-noise amplifier (LNA, Gain 30 dB) and the low pass filter (LPF, Mini-Circuits, SPL-21,4+, DC-22 MHz) to ensure that the APD output meets the minimum accuracy requirements of analog-to-digital converter (ADC). At the receiver, the FPGA (ALINX AX7325B) quantizes the signal into a digital signal using a 4-channel 12-bit ADC (ALINX, AL9627). After down-sampling, synchronization, channel estimation, and log-likelihood ratio (LLR) mapping, the digital signal is fed into the LDPC decoding IP core for decoding. The decoded bits are then checked for CRC.

Remark 1: The power consumption of the FPGA implementation of our real-time system depends on the specific FPGA
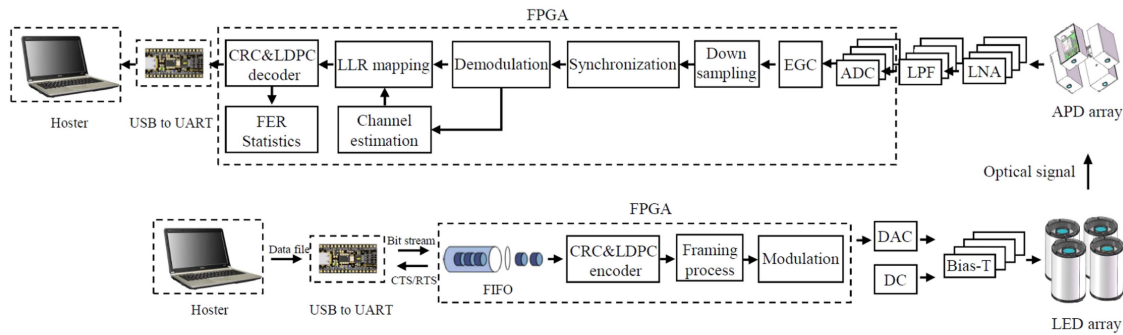
Fig. 7.   The block diagram in the data processing of real-time system.

TABLE I
THE BASE GRAPH DEFINITION

Base Graph	K_b	Supported m_b	Supported Z
0	22	$4 \leq m_b \leq 46$	$2 \leq Z \leq 384$
1	10	$4 \leq m_b \leq 42$	$2 \leq Z \leq 384$
2	9	$4 \leq m_b \leq 42$	$2 \leq Z \leq 128$
3	8	$4 \leq m_b \leq 42$	$2 \leq Z \leq 128$

model, the complexity of the implemented algorithms, and the operational conditions. In our implementation, the transmitter and receiver FPGA on-chip power is 0.732 W and 0.77 W, respectively. The majority of FPGA power consumption comes from dynamic power, including the clock, signal, and logic components.

Next, we will explain several key parts in detail.

1) 5G-NR LDPC Encoding and Decoding: The dynamic nature of W2A-OWC system is a fundamental characteristic. Underwater and surface OWC conditions are subject to rapid changes due to factors such as wavy water surface and terminal movement. One significant advantage of incorporating 5G-NR LDPC coding into these systems is the flexibility. Such coding technique allows for the optimization of transmission performance by adjusting the code rate based on real-time signal quality.

For 5G-NR LDPC, the code rate can be expressed as

$$C_r = \frac{K_b}{K_b + m_b}, \qquad (1)$$

where K_b and m_b denote the numbers of information and parity bits as a multiple of lifting factor Z, respectively. Table I shows the values of K_b for different base graphs along with the corresponding ranges for supported values of m_b and Z.

The 5G-NR LDPC BER performance is shown in Fig. 8. For each signal-to-noise ratio (SNR) point, groups of 10000 frames have been run until 10000 error bits have occurred. The decoder has been configured with a maximum of 40 iterations and early termination on parity pass. Additionally, OOK modulation and LLR demodulation have been adopted along with an additive white Gaussian noise (AWGN) channel. It is seen that the codes can operate in different SNR regimes, constituting a tradeoff between transmission efficiency and reliability.
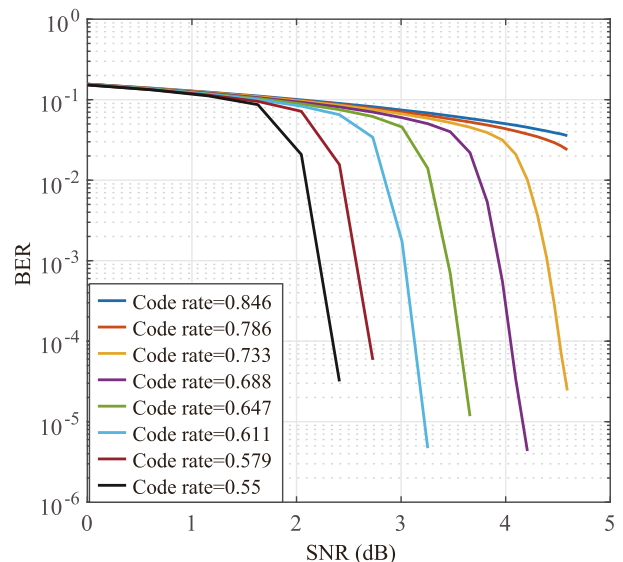

Fig. 8.   BER of 5G-NR LDPC versus SNR for different code rates.

2) Channel Estimation: After data frame synchronization, the aligned frame header serves as a training sequence for channel estimation, for not only the average signal intensity within the same frame but also the noise variance. The electrical-domain signals are assumed to be zero-mean and vary due to factors such as the low noise amplifier (LNA) and the ADC output bias, which are influenced by the system characteristics. Additionally, the shot noise of the APD, which is affected by strong outdoor background radiation, shows lower levels in the morning and evening, but higher levels at midday.

III. EXPERIMENTAL RESULTS

A. Laboratory Experiment

The experimental environment in a laboratory water tank of our real-time system is shown in Fig. 9. The transmitter is composed of $M = 4$ LEDs for diversity transmission, which are managed by an FPGA and a host computer. The receiver, located on a slide rail, consists of $N = 4$ APDs for diversity reception, coordinated by the FPGA and host computer. The wave maker and solar simulator are used to simulate disturbances in real W2A-OWC scenarios. The water tank is 3 m in long, 1 m in
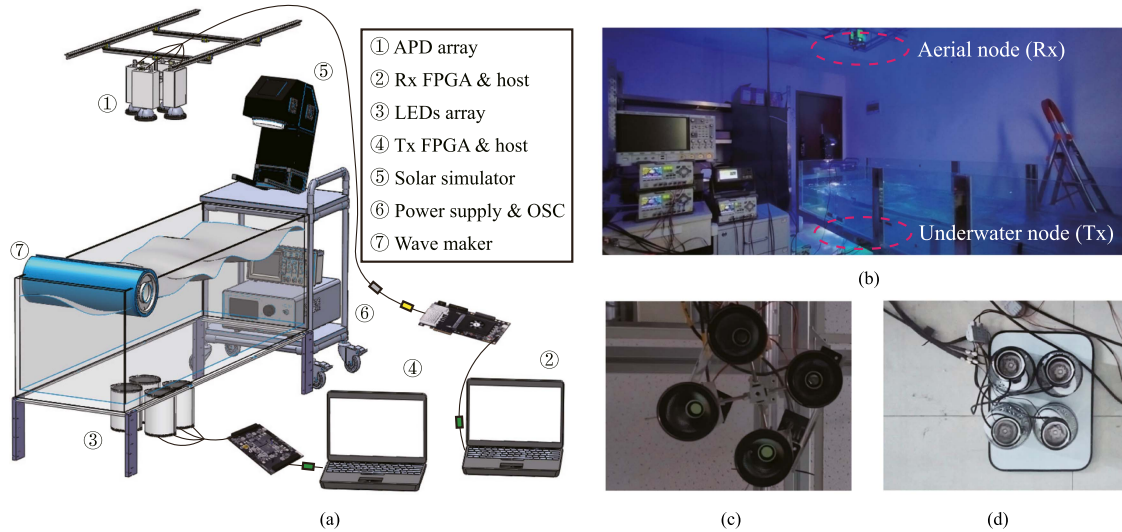
Fig. 9. The experimental environment in laboratory tank. (a) The experimental W2A-VLC system sketch. (b) The real scene of experiment setup. (c) The APD array. (d) The LED array.

wide, and 0.6 m in high. The LED is placed on the ground, 0.2 m from the bottom of the tank. The water depth inside the tank is maintained at 0.3 m. The receiver is mounted on an XY-slide, 2 m above the water surface. The attenuation coefficient of the tap water in the experiment is 0.16 m^{-1}, slightly exceeding that of clean ocean waters. Based on the scale on the water tank wall, the wavelength of the waves ranges from 2 cm to 8 cm, and the wave height ranges from 0.5 cm to 2 cm, approximately.

The system uses 0.846 and 0.55 as the maximum and minimum code rates, and a total of eight code rates are selected. To emulate outdoor conditions of low SNR, we remove the lens from the LED setup and reduce the strength of the DAC output. Such adjustment guarantees that the system works under conditions conducive to error frames, thereby simulating a more challenging communication environment. The complete system parameters are shown in Table II.

Fig. 10 shows the FER versus the code rate for different sizes of MIMO systems. Obviously, adopting MIMO strategy can significantly reduce the FER. When the system operates in SISO mode with $M = 1$ and $N = 1$, it exhibits an FER of 99% (92.61%) at a code rate of 0.846 (0.55). Such result indicates that although decreasing the code rate slightly enhances performance, the overall system performance is still poor. However, when the system operates with $M = 2$ and $N = 2$, the FER decreases to 78.19% at a code rate of 0.846 and to 26.48% at a code rate of 0.55. For the 3×3 MIMO system, the FER decreases to 19.49%; while for the 4×4 MIMO system, the FER is further decreases to 16.65%. This indicates a noticeable improvement in system reliability for larger MIMO configuration size.

Figs. 11 and 12 show the FER versus the code rate for different sizes SIMO and MISO systems, respectively. It is also shown that increasing the number of LEDs or APDs independently can lead to a reduction in the FER.

We have developed a prototype that includes a feedback link capable of adaptively adjusting the code rate of system.

TABLE II
EXPERIMENTAL PARAMETERS IN LABORATORY TANK

	Parameter	Value
System	Coding scheme	5G-NR LDPC, BG0
	LDPC rate	0.846, 0.786, 0.733, 0.688, 0.647, 0.611, 0.579, 0.55
	Length of data bits	1408
	Decoding algorithm	Min-sum algorithm
	Sampling rate	100 MSPS
	Air interface rate	5 Mbps
	Serial port baud rate	Tx: 1953125 Baud/s, Rx: 3676470 Baud/s
Transmitter	Total transmission frames	300000
	Depth under the water surface	0.5 m
	Divergence angle	120°
	Number of LEDs	4
	LED array configuration	Square vertices
Receiver	Height above the water surface	2 m
	FOV	70°
	Number of APDs	4
	APD array configuration	Square vertices
	Background radiation intensity	47 mW
	Attenuation coefficient	0.16 m^{-1}

A green LED at the receiver and two APDs each equipped with a corresponding band-pass filter at the transmitter are adopted to establish the feedback link. The code rate of the system is then determined by the measured real-time FER. The receiver monitors the FER based on the latest N_{FER} received data frames and two thresholds are employed. If the system FER falls below the lower threshold, the code rate is increased. If the FER surpasses the higher threshold, the code rate is decreased. When the FER lies within these two thresholds, the code rate
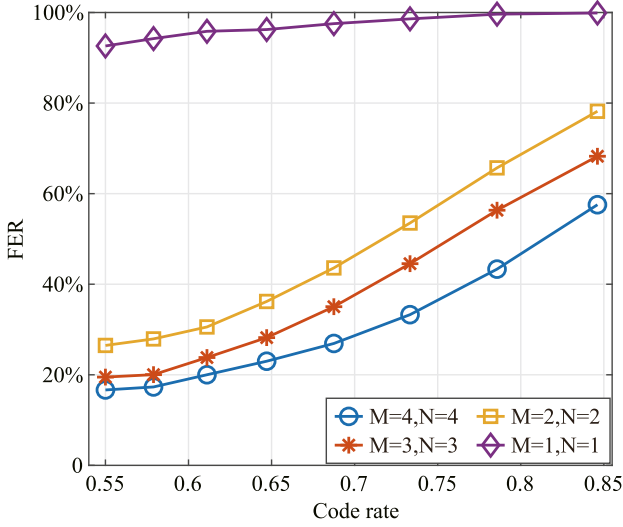
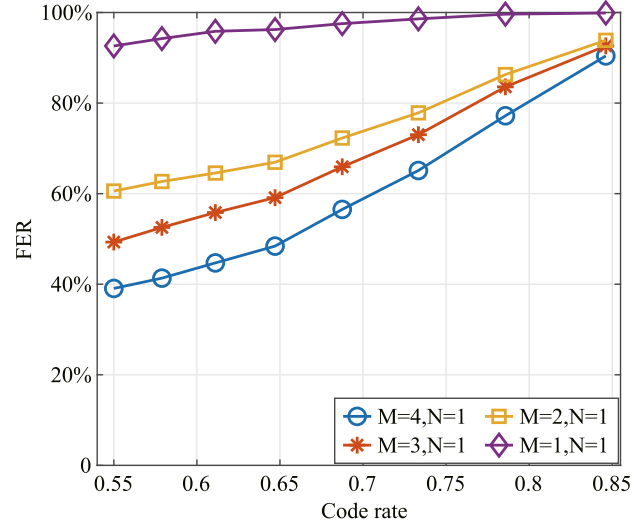Fig. 10. The FER versus the code rate for different sizes of MIMO systems.

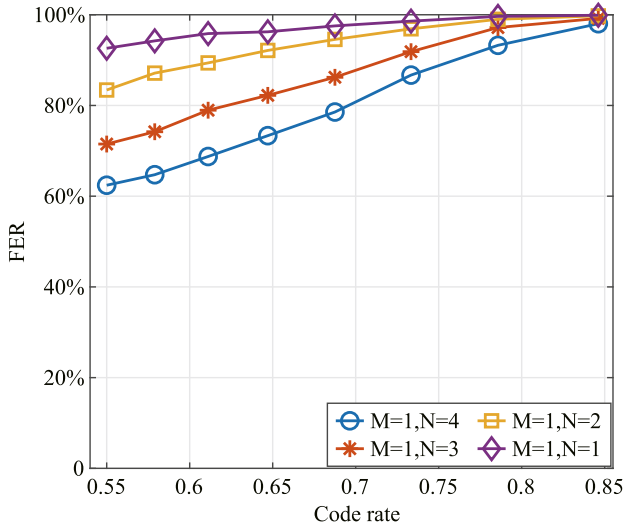Fig. 12. The FER versus the code rate for different sizes of MISO systems.

Fig. 11. The FER versus the code rate for different sizes of SIMO systems.
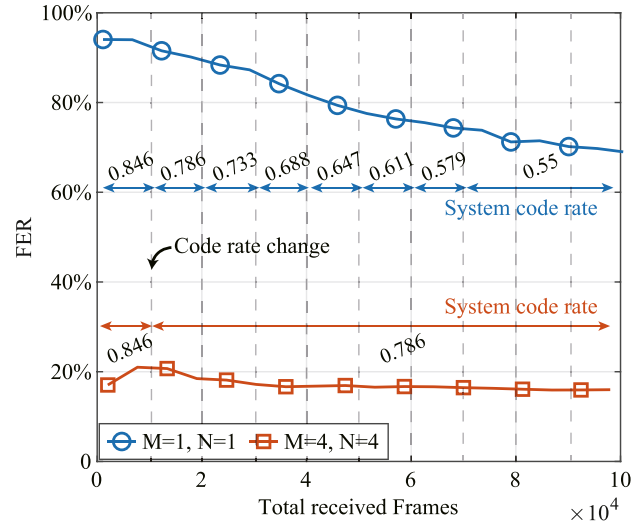

Fig. 13. The FER versus total received frames with feedback channel.

remains the same. At the receiver, each code rate corresponds to a specific 64-bit m-sequence. The transmitter determines the LDPC code rate by calculating the correlation value between the received signal and each m-sequence.

The code rate adaptation is evaluated in a laboratory water tank. We employ the integrated logic analyzer (ILA) IP core in FPGA to continuously monitor the overall FER and gather code rate data. The initial code rate is 0.846, with N_{FER} set to 10,000. Two thresholds are set to be 10% and 20%, respectively.

Fig. 13 shows the FER versus total received frames with feedback channel. In the SISO system, the channel conditions are notably poor, resulting in a high FER of 96.2% at a code rate of 0.846. Consequently, the system adaptively decreases the code rate to 0.786, which reduces the total FER to 93.5%. Finally, the system decreases the code rate to the minimum permissible rate of 0.55. After transmitting 100,000 frames, the total FER decreases to 71.1%. This result confirms that varying the code

rate in response to channel conditions effectively reduces the FER. In the 4×4 MIMO system, the FER at a code rate of 0.846 initially exceeds 20%. After reducing the code rate, the system successfully reduces the FER to a range between 10% and 20%. Subsequently, the system maintains such code rate for data transmission.

B. Outdoor Deep Pool Experiment

We further establish a W2A-OWC system in a deep wave pool, which is 3 m long, 5 m wide, and 5 m deep, as shown in Fig. 14(a). The top view of the deep pool is shown in Fig. 14(b). The experimental environment is shown in Fig. 14(c) and (d), where the aerial node and underwater node are mounted in the configuration shown in Figs. 1 and 5. The primary limiting factors for the transmission distance include the LED transmit power, as the light intensity decreases significantly over distance
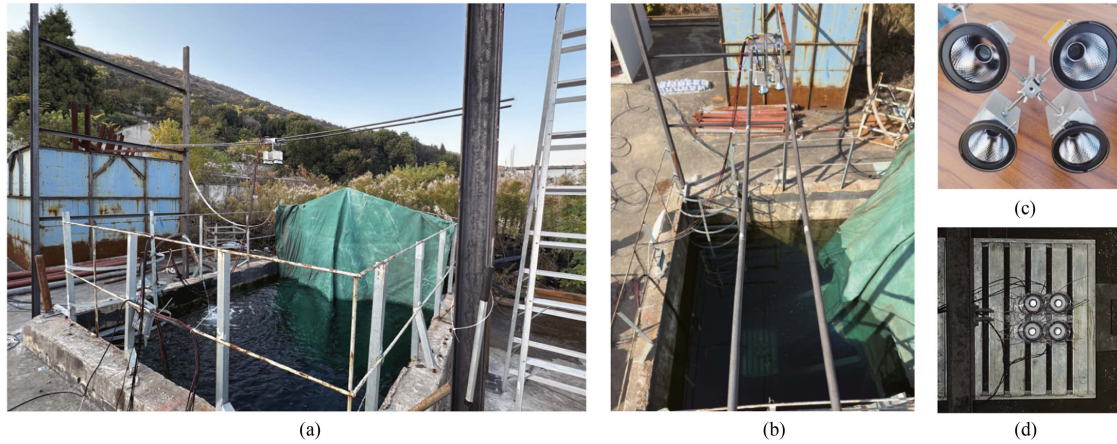
Fig. 14. The experimental environment in outdoor deep pool. (a) The overall scenario. (b) The top view. (c) The aerial node. (d) The underwater node.
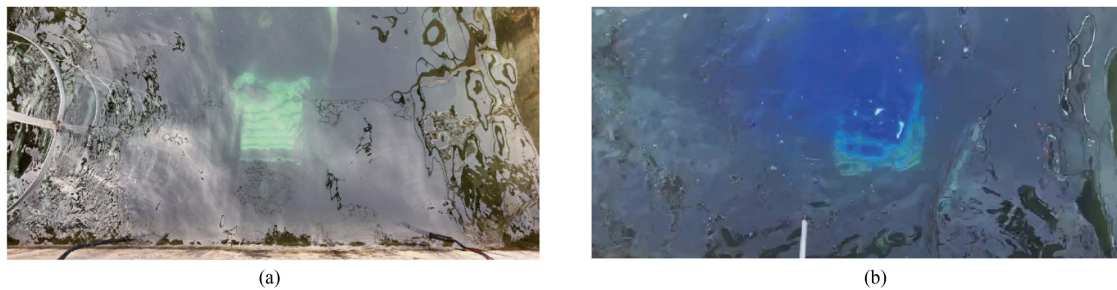

Fig. 15. The dynamic water surface in outdoor experiment. (a) Dynamic water surface when the underwater LEDs are off. (b) Dynamic water surface when the underwater LEDs emit blue light.

due to beam divergence and path attenuation. The dynamic water surface when the LEDs are off and emit blue light is shown in Fig. 15(a) and Fig. 15(b), respectively.

Another significant factor is the size of APD photosensitive area, which impacts the received signal strength. While increasing the APD photosensitive area could enhance the reception of signal light, it would also increase the intensity of background radiation received, thus raising the shot noise in the APD. This necessitates a more sophisticated optical antenna design to effectively separate signal light from ambient light. Additionally, enlarging the APD photosensitive area can degrade its bandwidth response, which is detrimental to support high-speed communication in future applications.

Furthermore, the difficulty of maintaining alignment between the transmitter and receiver also limits the increase in communication distance. Our current design lacks active tracking technology between the transmitter and receiver, relying solely on coarse alignment. In the future, developing more efficient cross-surface positioning techniques will be crucial, particularly for receivers located at high underwater depths.

Lastly, the water depth of the outdoor test pool, which is only 5 meters, is a limiting factor. This shallow depth restricts our ability to test longer transmission distances. As deeper waters might exhibit different signal propagation characteristics, it requires further research and optimization.

The structure of the test system is the same as that of the indoor real-time system. Note that the dynamic range of background

radiation is large and varies over time, resulting in differing experimental results at different time of the day. In real experiments, we conduct transmission tests only between 11 AM and 1 PM, where two data rates (0.846 and 0.579) suffice. The complete system parameters are shown in Table III.

The performance of the outdoor real-time system is depicted in Fig. 16. It is evident that increasing the MIMO system size and reducing the code rate both substantially enhance the FER performance. In outdoor experiments, the SISO configuration yields an FER of 93.4% at a code rate of 0.846. By augmenting the numbers of LEDs and APDs, the 4×4 MIMO configuration achieves an FER of 28.16%. Further reducing the system code rate to 0.579 significantly improves performance. Under the SISO setup, the FER is 89.3% at a code rate of 0.846. Increasing the numbers of LEDs and APDs to a 4×4 MIMO setup, the FER drops to 0.

The experimental results from indoor water tanks and outdoor deep pools indicate that the array transmission and reception scheme can exploit the weak spatial correlation under small-scale components in wave to create multiple independent transmission paths between the transmitter and receiver. This reduces the impact of channel fading caused by the random fluctuation of water surface, while increasing the number of LEDs and APDs can increase the total transmission and reception power. This is particularly important when the peak power of a single LED is limited and the photosensitive area of the APD is small, as it enhances the long-distance transmission capability of W2A-OWC
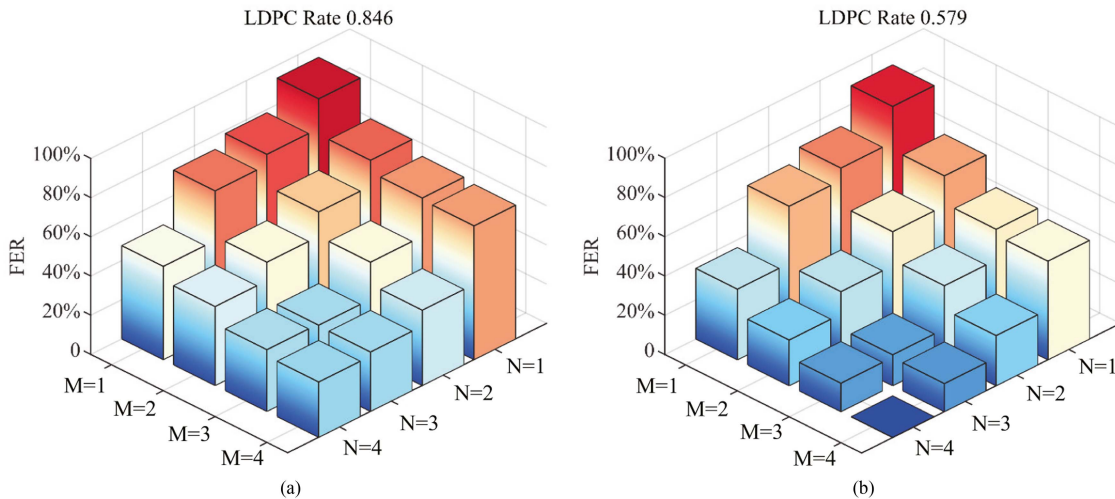
Fig. 16. The FER performance of the outdoor real-time system. (a) At LDPC code rate 0.846. (b) At LDPC code rate 0.579.

TABLE III
EXPERIMENTAL PARAMETER OF OUTDOOR DEEP POOL

	Parameter	Value
System	Coding scheme	5G-NR LDPC, BG0
	LDPC rate	0.846 / 0.579
	Length of data bits	1408
	Decoding algorithm	Min-sum algorithm
	Sampling rate	100 MSPS
	Air interface rate	5 Mbps
	Serial port baud rate	Tx: 1953125 Baud/s
		Rx: 3676470 Baud/s
Transmitter	Total transmission frames	100000
	Depth under the water surface	5 m
	Divergence angle	10°
	Number of LEDs	4
	LED array configuration	Square vertices
Receiver	Height above the water surface	3 m
	FOV	45°
	Number of APDs	4
	APD array configuration	Square vertices
	Background radiation intensity	243 mW
	Attenuation coefficient	0.12 m^{-1}

system. Moreover, increasing the number of LEDs and APDs can reduce the requirement for precise alignment, expanding the communication coverage area.

IV. CONCLUSION

In this work, we have realized an array-based FPGA real-time prototype of W2A-OWC system. The real-time system utilizes MIMO technology and 5G-NR LDPC codes to enhance data transmission stability, while spatial optical filtering reduces the impact of background radiation on the operating state of APDs. To assess the practical feasibility of the W2A-OWC system, we have conducted experiments in both indoor water tank and outdoor deep pool with strong background radiation. The experimental results demonstrate that compared to SISO system, a 4×4 MIMO system, achieves a significant reduction in FER from 93.4% to 28.16% at a code rate of 0.846, and from 89.3% to 0 at a code rate of 0.579. The W2A-OWC system can achieve error-free transmission under fluctuating water surface and strong background radiation, reaching distances of 5 m underwater and 3 m in the atmosphere.

REFERENCES

[1] M. C. Domingo, "An overview of the Internet of underwater things," *J. Netw. Comput. Appl.*, vol. 35, no. 6, pp. 1879–1890, Nov. 2012.

[2] Q. Wang, H.-N. Dai, Q. Wang, M. K. Shukla, W. Zhang, and C. G. Soares, "On connectivity of UAV-assisted data acquisition for underwater Internet of Things," *IEEE Internet Things J.*, vol. 7, no. 6, pp. 5371–5385, Jun. 2020.

[3] L.-K. Chen, Y. Shao, and Y. Di, "Underwater and water-air optical wireless communication," *IEEE/Optica J. Lightw. Technol.*, vol. 40, no. 5, pp. 1440–1452, Mar. 2022.

[4] D. Pompili and I. F. Akyildiz, "Overview of networking protocols for underwater wireless communications," *IEEE Commun. Mag.*, vol. 47, no. 1, pp. 97–102, Jan. 2009.

[5] Z. Zeng, S. Fu, H. Zhang, Y. Dong, and J. Cheng, "A survey of underwater optical wireless communications," *IEEE Commun. Surv. Tut.*, vol. 19, no. 1, pp. 204–238, Firstquarter 2017.

[6] J. Zhou, H. Jiang, P. Wu, and Q. Chen, "Study of propagation channel characteristics for underwater acoustic communication environments," *IEEE Access*, vol. 7, pp. 79438–79445, 2019.

[7] K. Takizawa, R. Suga, T. Matsuda, and F. Kojima, "Experiment on MIMO communications in seawater by RF signals," in *Proc. IEEE 93rd Veh. Technol. Conf.*, 2021, pp. 1–5.

[8] T. Lin, C. Gong, J. Luo, and Z. Xu, "Dynamic optical wireless communication channel characterization through air-water interface," in *Proc. IEEE/CIC Int. Conf. Commun. China*, 2020, pp. 173–178.

[9] M. S. Islam and M. F. Younis, "Analyzing visible light communication through air–water interface," *IEEE Access*, vol. 7, pp. 123830–123845, 2019.

[10] T. Lin et al., "Waving effect characterization for water-to-air optical wireless communication," *IEEE/Optica J. Lightw. Technol.*, vol. 41, no. 1, pp. 120–136, Jan. 2023.

[11] Y. Chen et al., "26m/5.5Gbps air-water optical wireless communication based on an OFDM-modulated 520-nm laser diode," *Opt. Exp.*, vol. 25, no. 13, pp. 14760–14765, Jun. 2017.

[12] H.-H. Lu et al., "A 400-Gb/s WDM-PAM4 OWC system through the free-space transmission with a water–air–water link," *Sci. Rep.*, vol. 11, no. 1, Nov. 2021, Art. no. 21431.

[13] Y. Shao, R. Deng, J. He, K. Wu, and L.-K. Chen, "Real-time 2.2-Gb/s water-air OFDM-OWC system with low-complexity transmitter-side DSP," *IEEE/Optica J. Lightw. Technol.*, vol. 38, no. 20, pp. 5668–5675, Oct. 2020.

[14] X. Sun et al., "Field demonstrations of wide-beam optical communications through water-air interface," *IEEE Access*, vol. 8, pp. 160480–160489, 2020.

[15] Y. Di, Y. Shao, and L.-K. Chen, "Real-time wave mitigation for water-air OWC systems via beam tracking," *IEEE Photon. Technol. Lett.*, vol. 34, no. 1, pp. 47–50, Jan. 2022.

[16] Y. Di, Y. Shao, and L. Chen, "Mitigation of wave-induced packet loss for water-air optical wireless communication by a tracking system," in *Proc. Opt. Fiber Commun. Conf. Exhib.*, 2021, pp. 1–3.

[17] C. J. Carver, Z. Tian, H. Zhang, K. M. Odame, A. Q. Li, and X. Zhou, "Amphilight: Direct air-water communication with laser light," *GetMobile: Mobile Comput. Commun.*, vol. 24, no. 3, pp. 26–29, Jun. 2021.

[18] I. E. Lee, Y. Guo, T. K. Ng, K.-H. Park, M.-S. Alouini, and B. S. Ooi, "Bandwidth enhancement of wireless optical communication link using a near-infrared laser over turbid underwater channel," in *Proc. Conf. Lasers Electro-Opt./Pacific Rim*, 2017, p. s1921.

[19] K. Tanaka, A. Kariya, F. Kobori, K. Shimada, S. Hayashida, and T. Kodama, "Demonstration of full-duplex and real-time transmission over 10m air and 1.2m water channel for completely invisible optical wireless communication systems," in *Proc. Photonic Netw. Devices*, 2023, paper NeW4B-2.

[20] X. Sun, M. Kong, C. Shen, C. H. Kang, T. K. Ng, and B. S. Ooi, "On the realization of across wavy water-air-interface diffuse-line-of-sight communication based on an ultraviolet emitter," *Opt. Exp.*, vol. 27, no. 14, pp. 19635–19649, Jul. 2019.

[21] C. J. Carver et al., "Air-water communication and sensing with light," in *Proc. 14th Int. Conf. Commun. Syst. Netw.*, 2022, pp. 371–374.